

# Modeling of turbulent particle and heat transport in helical plasmas based on gyrokinetic analysis

journal or publication title	Physics of Plasmas
volume	26
page range	012510
year	2019-01-28
URL	<a href="http://hdl.handle.net/10655/00012618">http://hdl.handle.net/10655/00012618</a>

doi: <https://doi.org/10.1063/1.5058720>



# **Modeling of turbulent particle and heat transport in helical plasmas based on gyrokinetic analysis**

S. Toda,<sup>1, a)</sup> M. Nakata,<sup>1, 2</sup> M. Nunami,<sup>1, 2</sup> A. Ishizawa,<sup>3</sup> T. -H. Watanabe,<sup>4</sup> and H. Sugama<sup>1, 2</sup>

<sup>1)</sup> *National Institute for Fusion Science, National Institutes of Natural Sciences, Toki, Gifu 509-5292, Japan*

<sup>2)</sup> *The Graduate University for Advanced Studies, Toki, Gifu 509-5292, Japan*

<sup>3)</sup> *Graduate School of Energy Science, Kyoto University, Gokasho, Uji, Kyoto, 611-0011, Japan*

<sup>4)</sup> *Department of Physics, Nagoya University, Furo-cho, Nagoya, Aichi, 464-8602, Japan*

(Dated: 3 February 2020)

The particle and heat transport driven by the ion temperature gradient instability in helical plasmas are investigated by the gyrokinetic analysis taking into account the kinetic electron response. High and low ion temperature plasma cases for the discharge in the Large Helical Device (LHD) are studied. Two types of the transport model with the lower computational cost to reproduce the nonlinear gyrokinetic simulation results within allowable errors are presented for application to quick transport analyses. The turbulent electron and ion heat diffusivity models are given in terms of the linear growth rate and the characteristic quantity for the linear response of zonal flows, while the model of the effective particle diffusivity is not obtained for flattened density profile observed in the LHD. The quasilinear flux model is also shown for the heat transport. The quasilinear flux models for the energy fluxes are found to reproduce the nonlinear simulation results at the accuracy similar to that of the heat diffusivity models. In addition, the quasilinear particle flux model, which is applicable to the transport analysis for LHD plasmas, is constructed. These turbulent reduced models enable to couple to the other simulation in the integrated codes for the LHD.

PACS numbers: 52.25.Fi, 52.35.Mw, 52.35.Ra, 52.55.Hc, 52.65.Tt

---

<sup>a)</sup>toda@nifs.ac.jp

## I. INTRODUCTION

A quantitative prediction of turbulent transport<sup>1,2</sup> is one of the most critical issues for realizing magnetic fusion energy. Recently, a large number of gyrokinetic simulations of the turbulent transport in toroidal plasmas have been performed<sup>3–9</sup>. The gyrokinetic analysis results in tokamak<sup>10–12</sup> and helical<sup>13,14</sup> plasmas have been compared with the experimental observation results. In tokamak plasmas, the transport simulation, which is directly coupled to gyrokinetic analyses at each time step, is globally performed<sup>15,16</sup>. The gyrokinetic simulation for helical plasmas consumes much larger computer resources than those for tokamak plasmas, because the former requires a large number of mesh points along field lines in order to resolve helical ripple structures. Since it is still not easy to couple the nonlinear gyrokinetic simulation with an integrated transport simulation code, especially for helical plasmas<sup>17</sup>, the predictive model, which can quickly approximate the nonlinear simulation results, is highly demanded. The predictive model for the turbulent transport with the lower computational cost enables to be incorporated with the other simulation codes (*e.g.* the neoclassical transport codes) in the integrated transport simulation for the Large Helical Device (LHD).

The GKV code<sup>18</sup> has been widely used to investigate the ion temperature gradient (ITG) mode and zonal flows in the LHD for studying the turbulent transport<sup>8,13,14,19–23</sup>. Gyrokinetic simulations using the adiabatic electron assumption are performed for the high and the low ion temperature LHD cases in shot number 88343<sup>24</sup>. The reduced model for the ion heat diffusivity was proposed<sup>14</sup> to quantitatively reproduce the nonlinear simulation results given by the turbulence simulation with adiabatic electrons. This reduced model is the function of the linear growth rate for the ITG mode and the zonal flow decay time<sup>25,26</sup>. The ion energy flux by this reduced model is in good agreement with the experimental results for the high- $T_i$  plasmas at  $t = 2.2\text{s}$ <sup>13,14</sup>. How to apply the reduced model of the turbulent ion heat diffusivity in the adiabatic electron condition to the transport code has been shown for helical plasmas<sup>22</sup>. The simulation in the kinetic electron condition shows the larger ion energy flux than the experimental results for the high- $T_i$  plasmas<sup>20</sup>. On the other hand, the electron and ion energy fluxes obtained from the simulation with kinetic electrons are close to those of the experimental results in the low- $T_i$  plasmas<sup>21</sup> at  $t = 1.8\text{s}$ . The simulation result with adiabatic electrons in the low- $T_i$  plasmas shows that the ITG mode becomes stable

around  $\rho(=r/a)=0.5$ . Kinetic electrons induce the enhancement of the linear growth rate of ITG modes<sup>5,20</sup>.

This work presents the predictive transport model for the particle and electron heat diffusivities in addition to the ion heat diffusivity, including the effect of kinetic electrons on the plasma instability. For the purpose, the gyrokinetic equations for both electrons and ions are solved to evaluate the diffusivities and fluxes of the heat and particle transport. To accurately evaluate the particle and electron heat transport, the simulation of the wider spatial domain and the finer spatial resolution is performed than those in the previous work<sup>23</sup>, where only the ion heat transport is estimated. The electron and ion heat diffusivity models are presented, to reproduce the nonlinear simulation results within allowable errors in terms of the linear growth rates and the linear response of zonal flows. The quasilinear flux models are presented to approximately reproduce the particle transport in addition to the heat transport obtained by the gyrokinetic simulations.

## II. NONLINEAR GYROKINETIC SIMULATION RESULTS

The turbulence driven by the microinstabilities in LHD plasmas is studied, using the gyrokinetic local flux tube code GKV<sup>18</sup>. The electromagnetic gyrokinetic equations are solved for both electrons and ions<sup>20</sup> in this article. The temperature and density profiles, and field configuration obtained from the LHD experimental results for the shot number 88343<sup>24</sup> of the high- $T_i$  plasmas at  $t = 2.2$ s and of the low- $T_i$  plasmas at  $t = 1.8$ s and 1.9s are used. This is because the experimentally observed fluctuations in these plasmas for the LHD are driven by ITG mode<sup>8</sup> and these plasmas are chosen as the representative plasmas for study of the ITG mode. The validation studies are progressed for the adiabatic electron approximation<sup>13,14,22</sup> and kinetic electron response<sup>20,21</sup> by using the plasma profiles and field configurations for the shot number 88343 of the high- $T_i$  and low- $T_i$  plasmas in the LHD. The major radii of the LHD plasmas are given by  $R = 3.75$ m for the high- $T_i$  plasmas and  $R = 3.6$ m for the low- $T_i$  plasmas. In the low- $T_i$  plasmas, the magnetic field configuration is shifted more inward than in the high- $T_i$  plasmas. The generation of zonal flows can be enhanced in the inward shifted configuration<sup>27</sup>. The  $\beta(=2\mu_0 n(T_e + T_i)/B^2)$  values is 0.3% at  $\rho = 0.65$  for the high- $T_i$  plasmas and 0.2% at  $\rho = 0.68$  for the low- $T_i$  plasmas, where  $\mu_0$  is the vacuum permeability. Note that the reduced models in this study are valid for

the low- $T_i$  and high- $T_i$  plasmas in the LHD #88343 discharge. Transport simulation by the reduced model<sup>14</sup> with the adiabatic electron condition for the high- $T_i$  plasmas of the other shot than the shot number 88343 in the LHD has been performed and the comparable ion temperature profile to the experimental result is obtained<sup>28</sup>. The grid numbers used for the wavenumber variables,  $\tilde{k}_x$ ,  $\tilde{k}_y$ , the parallel real space variable, the parallel and perpendicular velocity space variables are 41, 12, 512, 64 and 16, where  $\tilde{k}_x(= k_x \rho_i)$  and  $\tilde{k}_y(= k_y \rho_i)$  are the normalized radial and poloidal wavenumbers, respectively, and  $\rho_i$  is the ion gyroradius. The grid numbers in the present simulations are smaller than those in the simulation of Refs. 20 and 21 in order to perform nonlinear simulations at more radial points for modeling the particle and heat transport here than in Ref. 21. However, it is verified that the values of the electron and ion energy fluxes, and the particle flux obtained in this study have almost the same level of accuracy as those in Refs. 20 and 21. For the high- $T_i$  plasmas, the nonlinear GKV simulations are performed at the ten radial points in the region  $0.46 \leq \rho \leq 0.80$ , while they are carried out at the ten radial points in  $0.65 \leq \rho \leq 0.80$  for the low- $T_i$  plasmas. The time evolutions of the electron and ion energy fluxes, and the particle flux at  $\rho = 0.65$  for the high- $T_i$  plasmas are shown in Fig. 1(a) and (b), respectively. The energy fluxes for the species  $j$  are  $Q_j(= Q_j^{es} + Q_j^{em})$ , where the electrostatic part is  $Q_j^{es} = Re \left\langle \sum_{\mathbf{k}_\perp} \int (m_j v_\parallel^2 + \mu_0 B) h_{j\mathbf{k}_\perp} J_{0j} d^3 v (-ik_y \phi_{\mathbf{k}_\perp} / B)^* / 2 \right\rangle$  and the electromagnetic part is  $Q_j^{em} = Re \left\langle \sum_{\mathbf{k}_\perp} \int v_{tj} v_\parallel (m_j v_\parallel^2 + \mu_0 B) h_{j\mathbf{k}_\perp} J_{0j} d^3 v (ik_y A_{\parallel \mathbf{k}_\perp} / B)^* / 2 \right\rangle$ <sup>20</sup>. Here,  $m_j$ ,  $v_\parallel$ ,  $B$ ,  $v$ ,  $\phi$  and  $A_{\parallel \mathbf{k}_\perp}$  are the mass for the species  $j$ , the parallel velocity, the magnetic field strength, the velocity, the electrostatic potential and the electromagnetic potential. The term  $h_{j\mathbf{k}_\perp}$  represents the non-adiabatic part of the perturbed part in the gyro-center distribution function,  $J_{0j}(= J_0(\rho_j k_\perp))$  is the zeroth order Bessel function and  $\mathbf{k}_\perp = (k_x, k_y)$ , where  $\rho_j = m_j v_{tj} / (eB)$  with  $v_{tj} = \sqrt{T_j / m_j}$  for the species  $j$ . The bracket  $\langle \rangle$  denotes the averaged values along the magnetic field line. The particle flux is  $\Gamma(= \Gamma^{es} + \Gamma^{em})$ , where the electrostatic part is  $\Gamma^{es} = Re \left\langle \sum_{\mathbf{k}_\perp} \int h_{j\mathbf{k}_\perp} J_{0j} d^3 v (-ik_y \phi_{\mathbf{k}_\perp} / B)^* / 2 \right\rangle$  and the electromagnetic part is  $\Gamma^{em} = Re \left\langle \sum_{\mathbf{k}_\perp} \int v_{ti} v_\parallel h_{j\mathbf{k}_\perp} J_{0j} d^3 v (ik_y A_{\parallel \mathbf{k}_\perp} / B)^* / 2 \right\rangle$ . The value of time  $t$  is normalized by  $R / v_{ti}$ . The saturation of the electron and ion energy fluxes, and the particle flux is confirmed. The ratios of the electromagnetic contributions  $Q_e^{em}$ ,  $Q_i^{em}$  and  $\Gamma^{em}$  to the electron and ion energy fluxes  $Q_e$ ,  $Q_i$  and the particle flux  $\Gamma$  are examined. It is confirmed that the time averaged values of  $Q_e^{em} / Q_e$ ,  $Q_i^{em} / Q_i$  and  $\Gamma^{em} / \Gamma$  become small and are 4.8%, -0.77% and 9.0%, respectively. The averaged values of the electron and ion energy fluxes and the

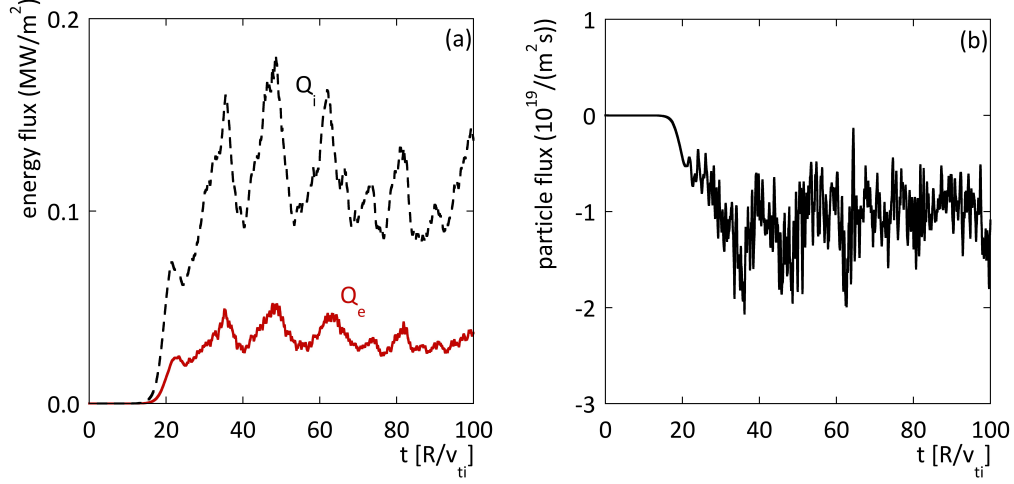


FIG. 1. Time evolutions of (a) the energy fluxes and (b) the particle flux at  $\rho = 0.65$  for the high- $T_i$  plasma case. The solid and dashed curves in (a) represent the electron and ion energy fluxes, respectively.

particle flux per unit area at  $\rho = 0.65$  in the time interval  $50 < t < 100$  for the high- $T_i$  plasmas are  $0.036 \text{ MW/m}^2$ ,  $0.11 \text{ MW/m}^2$  and  $-1.0 \times 10^{19}/(\text{m}^2\text{s})$ , respectively. In Fig. 2, the values of the time-averaged ion heat diffusivity  $\bar{\chi}_i$  obtained from the present simulations are compared with those from the simulations under the adiabatic electron condition, where the ion heat diffusivity  $\chi_i$  is defined by  $\chi_i = -Q_i/(n\partial T_i/\partial r)$ , the bar  $\bar{\phantom{x}}$  represents the average over the time interval of the nonlinear saturation phase. The values of  $\bar{\chi}_i$  from the present simulation are close to those in the adiabatic electron condition at  $\rho = 0.5$ . At  $\rho > 0.6$ , the values of  $\bar{\chi}_i$  from the present simulations are found to be two or three times larger than those obtained from the simulations in the adiabatic electron condition. The time evolutions of the squared turbulent potential fluctuation,  $\mathcal{T} \left( = \sum_{\tilde{k}_x, \tilde{k}_y \neq 0} \left\langle \left| \tilde{\phi}_{\tilde{k}_x, \tilde{k}_y} \right|^2 \right\rangle / 2 \right)$  and the squared zonal flow potential,  $\mathcal{Z} \left( = \sum_{\tilde{k}_x} \left\langle \left| \tilde{\phi}_{\tilde{k}_x, \tilde{k}_y=0} \right|^2 \right\rangle / 2 \right)$  at  $\rho = 0.65$  are examined, where  $\tilde{\phi}$  is the electrostatic potential fluctuation which is defined as  $\tilde{\phi} = \phi/(T_i \rho_i/(eR))$ . The nonlinear saturation is seen in the time evolution of  $\mathcal{T}$  and  $\mathcal{Z}$ . It is found that the ratio of  $\bar{\mathcal{Z}}$  to  $\bar{\mathcal{T}}$  in the kinetic electron condition is 0.19 and smaller than that in the adiabatic electron condition, 0.25, at  $\rho = 0.65$  for the high- $T_i$  plasmas. This result can be explained from the effect of trapped electrons which reduce the zonal flow generation<sup>25</sup>.

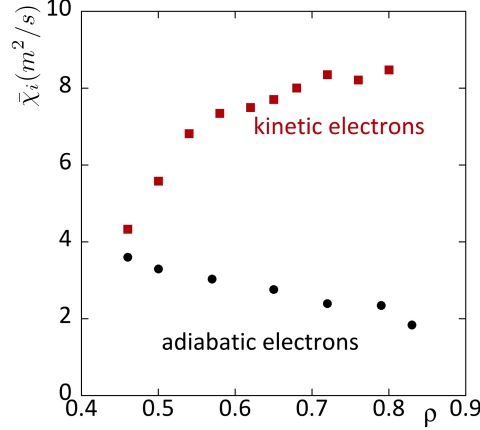


FIG. 2. Radial profiles of the time-averaged ion heat diffusivity  $\bar{\chi}_i$  obtained by the nonlinear simulations for the cases of kinetic electrons (the boxes) and adiabatic electrons (the circles)

### III. TRANSPORT MODEL BASED ON NONLINEAR SIMULATION RESULTS

Parameter ranges, in which the nonlinear simulations are performed, are shown in Table I, where  $R/L_{T_e}$  is the normalized electron temperature gradient,  $R/L_{T_i}$  is the normalized ion temperature gradient,  $R/L_n$  is the normalized density gradient and  $q$  is the safety factor. Here,  $L_{T_e} = -T_e/(\partial T_e/\partial r)$ ,  $L_{T_i} = -T_i/(\partial T_i/\partial r)$  and  $L_n = -n/(\partial n/\partial r)$ . These parameter ranges correspond to the LHD experimental results for the high- $T_i$  and low- $T_i$  plasmas. The nonlinear simulation results for the radial profiles of the electron and ion energy fluxes, and the particle flux are shown in Fig. 3. The normalized transport coefficients  $\bar{\chi}_e/\chi_i^{GB}$  and  $\bar{\chi}_i/\chi_i^{GB}$  obtained from the nonlinear simulations are compared with the model functions  $\mathcal{F}_e$  and  $\mathcal{F}_i$  of  $\bar{\mathcal{T}}$  and  $\bar{\mathcal{Z}}$  in Fig. 4, where  $\chi_i^{GB} (= \rho_i^2 v_{ti}/R)$  is the gyroBohm diffusivity. The simulation results for the ion heat diffusivity are well fitted by the model function<sup>14</sup>

$$\frac{\bar{\chi}_i}{\chi_i^{GB}} = \mathcal{F}_i(\bar{\mathcal{T}}, \bar{\mathcal{Z}}) \equiv \frac{C_{1i} \bar{\mathcal{T}}^{\alpha_i}}{C_{2i} + \bar{\mathcal{Z}}^{1/2} / \bar{\mathcal{T}}}, \quad (1)$$

with  $\alpha_i = 0.41$ ,  $C_{1i} = 0.13$  and  $C_{2i} = 4.9 \times 10^{-2}$ . The relative error for fitting  $\bar{\chi}_i/\chi_i^{GB}$  by  $\mathcal{F}_i$  is 0.15, where the relative error is defined as the root mean square of  $[(\bar{\chi}_i/\chi_i^{GB})/\mathcal{F}_i - 1]$ . On the other hand, the simulation results for the electron heat diffusivity are well reproduced by the model function

$$\frac{\bar{\chi}_e}{\chi_i^{GB}} = \mathcal{F}_e(\bar{\mathcal{T}}, \bar{\mathcal{Z}}) \equiv \frac{C_{1e} \bar{\mathcal{T}}^{\alpha_e}}{C_{2e} + \bar{\mathcal{Z}}^\xi / \bar{\mathcal{T}}}. \quad (2)$$



TABLE I. Parameter ranges in the nonlinear simulations

$\rho$	0.46 to 0.80
$q$	1.2 to 2.2
$R/L_{T_i}$	6.6 to 16
$R/L_{T_e}$	4.6 to 15
$R/L_n$	-1.0 to 1.9

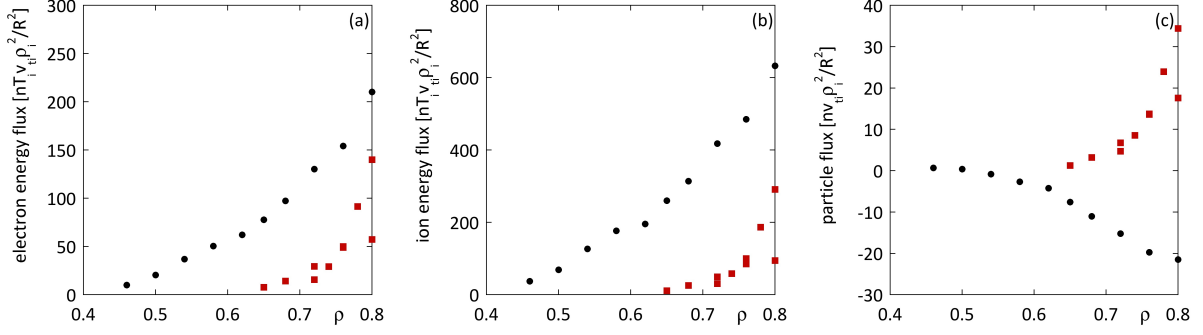


FIG. 3. The radial profiles of the (a) electron and (b) ion energy fluxes normalized by  $nT_i v_{ti} \rho_i^2 / R^2$  and the radial profiles of (c) the particle flux normalized by  $nv_{ti} \rho_i^2 / R^2$ . The circle and the box marks correspond to the simulation results in the high- $T_i$  and the low- $T_i$  plasmas, respectively.

with  $\alpha_e = 0.19$ ,  $C_{1e} = 6.8 \times 10^{-2}$ ,  $C_{2e} = 2.1 \times 10^{-2}$  and  $\xi = 0.10$ . The relative error for fitting  $\bar{\chi}_e / \chi_i^{GB}$  by  $\mathcal{F}_e$  is 0.079. Note that the exponent  $\xi = 0.10$  for  $\bar{\mathcal{Z}}$  in  $\mathcal{F}_e$  is smaller than the value  $1/2$  for  $\bar{\mathcal{Z}}$  in  $\mathcal{F}_i$ . We find that the poloidal wavenumber spectra of the  $Q_e$  take peaks at larger  $\tilde{k}_y$  values than those of the  $Q_i$ . The effect of zonal flows is considered to be more effective for lower wavenumbers and accordingly it is to be weaker for  $\bar{\chi}_e / \chi_i^{GB}$  than for  $\bar{\chi}_i / \chi_i^{GB}$ . In this study, the particle diffusivity model is not shown because the typical density profile in the LHD is flattened or hollow<sup>24</sup>. When the density gradient fluctuates around zero, it is difficult to obtain accurate values of the effective particle diffusivity  $D(= -\Gamma / (\partial n / \partial r))$ .

#### IV. HEAT DIFFUSIVITY MODELS BASED ON LINEAR SIMULATION RESULTS

In this section, the heat diffusivity models are given in terms of the linear simulation results, such as the quantity related with the mixing length estimate,  $\mathcal{L} \left( \equiv \int (\tilde{\gamma}_{\tilde{k}_y} / \tilde{k}_y^2) d\tilde{k}_y \right)$ <sup>29</sup>

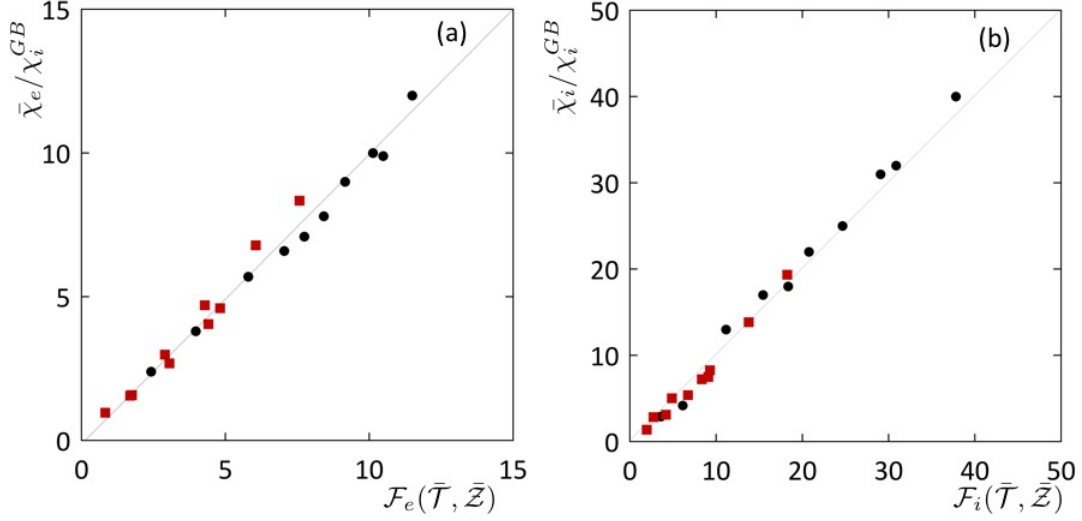


FIG. 4. Comparison of (a)  $\bar{\chi}_e/\chi_i^{GB}$  and (b)  $\bar{\chi}_i/\chi_i^{GB}$  from the nonlinear gyrokinetic simulation with the model functions  $\mathcal{F}_e(\bar{\mathcal{T}}, \bar{\mathcal{Z}})$  and  $\mathcal{F}_i(\bar{\mathcal{T}}, \bar{\mathcal{Z}})$ . The circles and the boxes show the results in high- $T_i$  and low- $T_i$  plasmas, respectively.

and the zonal flow decay time<sup>26</sup>, by adapting the method used when the reduced model for the ion heat diffusivity for the adiabatic electron condition was proposed<sup>14</sup>. Here,  $\tilde{\gamma}_{\tilde{k}_y}(=\gamma_{\tilde{k}_y}/(v_{ti}/R))$  is the linear growth rate at each  $\tilde{k}_y$ . The nonlinear simulation results,  $\bar{\mathcal{T}}$  and  $\bar{\mathcal{Z}}$  in the model functions (1) and (2), are represented by the linear simulation results. The instabilities, which are found in the condition for the high- $T_i$  and low- $T_i$  plasmas, are identified as the ITG modes, because the real frequencies are negative and the mode rotates in the ion diamagnetic direction. The quantity related with the mixing length estimate  $\mathcal{L}$  is obtained by integrating  $\tilde{\gamma}_{\tilde{k}_y}/\tilde{k}_y^2$  over the poloidal wavenumber region which is typically given as  $0.05 \leq \tilde{k}_y \leq 1.0$ . For the high- $T_i$  plasmas, the ITG mode is unstable in the radial region  $0.06 \leq \rho \leq 0.80$  under the kinetic electron condition and the resultant values of  $\mathcal{L}$  are several times larger than those in the adiabatic electron case where the ITG mode is unstable in the region  $\rho > 0.6$ . On the other hand, for the low- $T_i$  plasmas with kinetic electrons, the ITG mode becomes unstable in the region  $\rho \geq 0.65$ . The radial region where the ITG mode is unstable for the kinetic electron case is wider than for the adiabatic electron case. Figure 5 shows the relation between the turbulence fluctuation  $\bar{\mathcal{T}}$  and the quantity related with the mixing length estimate,  $\mathcal{L}$ . The turbulence fluctuation  $\bar{\mathcal{T}}$  is approximated by

$$\bar{\mathcal{T}} = C_T \mathcal{L}^a, \quad (3)$$

with the coefficients  $C_T = 6.6 \times 10$  and  $a = 1.6$ . The zonal flow fluctuation  $\bar{\mathcal{Z}}$  is represented by the zonal flow decay time and  $\mathcal{L}$ . The linear zonal flow response function is defined by  $\mathcal{R}_{\tilde{k}_x}(t) \equiv \langle \tilde{\phi}_{\tilde{k}_x, \tilde{k}_y=0}(t) \rangle / \langle \tilde{\phi}_{\tilde{k}_x, \tilde{k}_y=0}(t=0) \rangle$ . The linear zonal flow response depends on the magnetic field configuration, but it does not depend on the electron and ion temperature gradients, and the density gradient. Note that the zonal flow response function for  $\tilde{k}_x = 0.25$  is used to evaluate the representative values of the zonal flow decay time, because there are peaks of the wavenumber spectra around  $\tilde{k}_x = 0.25$  in the nonlinear simulation results examined here. To study the correlation between  $\mathcal{R}_{\tilde{k}_x}(t)$  and the fluctuation of zonal flows  $\bar{\mathcal{Z}}$ , the zonal flow decay time<sup>26</sup> is employed. The zonal flow decay time is defined by  $\tau_{ZF} \equiv \int_0^{\tau_f} dt \mathcal{R}_{\tilde{k}_x}(t)$ , where the upper limit  $\tau_f$  in the integral is set to  $\tau_f = 30R/v_{ti}$ . It is confirmed that helical magnetic structure in the inward-shifted field configuration enhances the zonal flow generation<sup>27</sup>. Therefore, the zonal flow decay time in the low- $T_i$  plasmas has the tendency to be larger than that in the high- $T_i$  plasmas for which the configuration is outward-shifted. The linear zonal flow response for the kinetic electron case is different from that for the adiabatic electron case, and the details are explained in Ref. 23. The squared zonal flow fluctuation  $\bar{\mathcal{Z}}$  is approximated by the linear simulation results,

$$\frac{\bar{\mathcal{Z}}^b}{\bar{\mathcal{T}}^c} = C_z \tilde{\tau}_{ZF}, \quad (4)$$

where  $C_z = 0.19$ ,  $b = 0.16$  and  $c = 0.27$  and  $\tilde{\tau}_{ZF} = \tau_{ZF}/(R/v_{ti})$ . The comparison of  $\bar{\mathcal{Z}}^{0.16}/\bar{\mathcal{T}}^{0.27}$  with  $0.19\tilde{\tau}_{ZF}$  is shown in Fig. 6. The circles and boxes represent the simulation results in the high- $T_i$  and low- $T_i$  plasmas, respectively.

When we rewrite Eqs. (2) and (1) using Eqs. (3) and (4), the electron and ion heat diffusivities are represented in terms of the linear simulation results,  $\mathcal{L}$  and  $\tilde{\tau}_{ZF}$  as

$$\frac{\chi_e^{model}}{\chi_i^{GB}} = \frac{A_{1e} \mathcal{L}^{B_{1e}}}{A_{2e} + \tilde{\tau}_{ZF}^{B_{2e}} / \mathcal{L}^{B_{3e}}}, \quad (5)$$

and

$$\frac{\chi_i^{model}}{\chi_i^{GB}} = \frac{A_{1i} \mathcal{L}^{B_{1i}}}{A_{2i} + \tilde{\tau}_{ZF}^{B_{2i}} / \mathcal{L}^{B_{3i}}}, \quad (6)$$

where the coefficients are given by  $A_{1e} = C_{1e} C_T^{\alpha_e+1-c\xi/b} C_z^{-\xi/b} = 1.3 \times 10$ ,  $A_{2e} = C_{2e} C_T^{1-c\xi/b} C_z^{-\xi/b} = 2.0$ ,  $A_{1i} = C_{1i} C_T^{\alpha_i+1-c/(2b)} C_z^{-1/(2b)} = 2.6 \times 10^2$  and  $A_{2i} = C_{2i} C_T^{1-c/(2b)} C_z^{-1/(2b)} = 1.8 \times 10$ . The exponents are given by  $B_{1e} = \alpha_e a = 0.30$ ,  $B_{2e} = \xi/b = 0.62$ ,  $B_{3e} = a(1 - c\xi/b) = 0.63$ ,  $B_{1i} = \alpha_i a = 0.66$ ,  $B_{2i} = 1/(2b) = 3.1$  and  $B_{3i} = a(1 - c/(2b)) = 0.26$ . The normalized electron and ion heat diffusivities  $\bar{\chi}_e/\chi_i^{GB}$  and  $\bar{\chi}_i/\chi_i^{GB}$  obtained from the nonlinear simulation

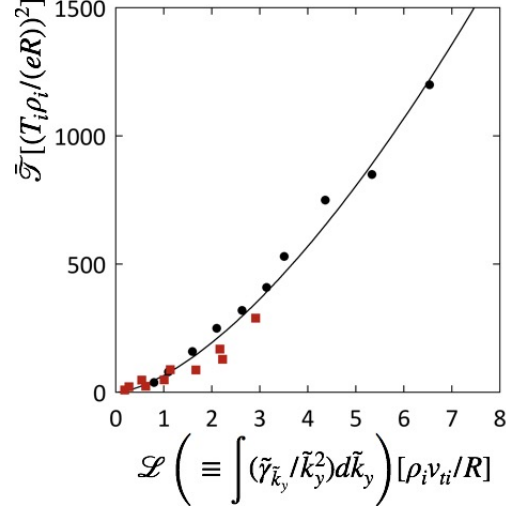


FIG. 5. Relation of the time-averaged turbulent fluctuation  $\bar{\mathcal{T}}$  and the quantity related with the mixing length estimate,  $\mathcal{L}$ . The circles and the boxes represent the results for the high- $T_i$  and low- $T_i$  plasmas, respectively.

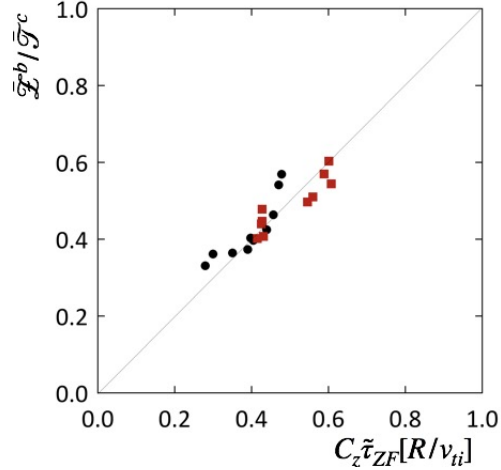


FIG. 6. The plots are shown for the comparison of  $\bar{\mathcal{Z}}^b / \bar{\mathcal{T}}^c$  with  $C_Z \tilde{\tau}_{ZF}$ , where  $b = 0.16$ ,  $c = 0.27$  and  $C_Z = 0.91$ . The circles show the simulation results for the high- $T_i$  plasmas and the boxes represent those in the low- $T_i$  plasmas.

are compared with the model predictions  $\bar{\chi}_e^{model} / \chi_i^{GB}$  and  $\bar{\chi}_i^{model} / \chi_i^{GB}$  in Fig. 7(a) and (b), respectively, where the circles and the boxes show the results in high- $T_i$  and low- $T_i$  plasmas. The heat diffusivity models reproduce the nonlinear simulation results  $\bar{\chi}_e / \chi_i^{GB}$  within the relative error 0.21 and  $\bar{\chi}_i / \chi_i^{GB}$  within the relative error 0.20.

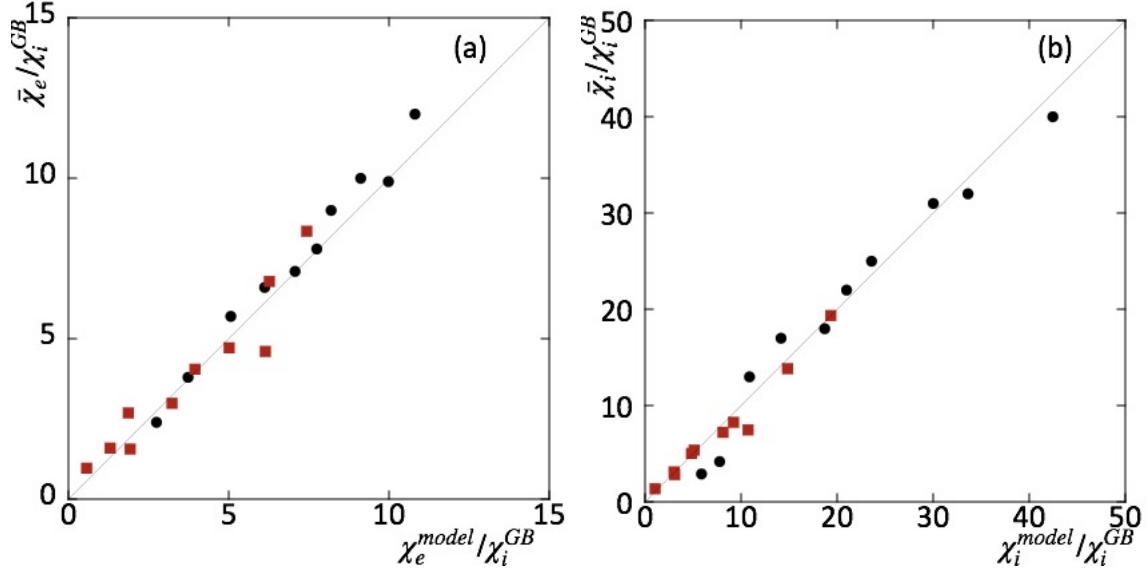


FIG. 7. The comparison of the electron and ion heat diffusivity,  $\bar{\chi}_e/\chi_i^{GB}$  and  $\bar{\chi}_i/\chi_i^{GB}$ , obtained from the nonlinear simulation with the model predictions of Eq. (5),  $\chi_e^{model}/\chi_i^{GB}$  and Eq. (6),  $\chi_i^{model}/\chi_i^{GB}$ . The circles and the boxes show the results for high- $T_i$  and low- $T_i$  plasmas, respectively.

## V. QUASILINEAR FLUX MODELS FOR PARTICLE AND HEAT TRANSPORT

In this section, the quasilinear models<sup>30–33</sup> are constructed for both the particle and the energy fluxes. In the quasilinear flux formulation<sup>30,31</sup>, the particle and energy fluxes are written as

$$\tilde{\Gamma}^{QL} = C_\Gamma \int \frac{\tilde{\Gamma}_{\tilde{k}_y}^{lin}}{\langle |\tilde{\phi}_{\tilde{k}_y}^{lin}|^2 \rangle} \langle |\tilde{\phi}_{\tilde{k}_y}^{NL}|^2 \rangle d\tilde{k}_y \quad (7)$$

and

$$\tilde{Q}_j^{QL} = C_{Q_j} \int \frac{\tilde{Q}_{j,\tilde{k}_y}^{lin}}{\langle |\tilde{\phi}_{\tilde{k}_y}^{lin}|^2 \rangle} \langle |\tilde{\phi}_{\tilde{k}_y}^{NL}|^2 \rangle d\tilde{k}_y \quad (8)$$

for the species  $j$ , where the quantities with the superscripts *lin* and *NL* represent the linear and nonlinear simulation results. Here, the tilde~represents the normalization of the energy and particle fluxes by the values of  $nT_i v_{ti} \rho_i^2 / R^2$  and  $n v_{ti} \rho_i^2 / R^2$ , respectively. The saturated intensity of the electrostatic potential fluctuation obtained from the nonlinear simulation,

$\langle |\tilde{\phi}_{\tilde{k}_y}^{NL}|^2 \rangle$ , is well fitted with the model function of  $\tilde{\gamma}_{\tilde{k}_y}/\tilde{k}_y^2$  and the zonal flow decay time  $\tilde{\tau}_{ZF}$ ,

$$\langle |\tilde{\phi}_{\tilde{k}_y}|^2 \rangle^{model} = \frac{C_{q1}(\tilde{\gamma}_{\tilde{k}_y}/\tilde{k}_y^2)^{\alpha_{q1}}}{C_{q2} + \tilde{\tau}_{ZF}^{\alpha_{ZF}}/(\tilde{\gamma}_{\tilde{k}_y}/\tilde{k}_y^2)^{\alpha_{q2}}} \quad (9)$$

at each  $\tilde{k}_y$ , where the parameters are  $C_{q1} = 1.0 \times 10^2$ ,  $C_{q2} = 9.2 \times 10^{-4}$ ,  $\alpha_{q1} = 0.54$ ,  $\alpha_{q2} = 0.12$  and  $\alpha_{ZF} = 1.6$ . To give the quasilinear flux models  $\tilde{\Gamma}_{ql}^{model}$  and  $\tilde{Q}_{j,ql}^{model}$  for the species  $j$ , the model function (9) is substituted into  $\langle |\tilde{\phi}_{\tilde{k}_y}^{NL}|^2 \rangle$  in Eqs. (7) and (8). When the relative errors of the fluxes at each  $\tilde{k}_y$  and the total fluxes integrated over the  $\tilde{k}_y$  space are minimized between the nonlinear simulation results and the quasilinear flux models, the fitting parameters are determined as  $C_{Q_e} = 0.78$ ,  $C_{Q_i} = 0.58$  and  $C_\Gamma = 0.73$ . The fluxes from the nonlinear simulation (a)  $\tilde{\Gamma}^{NL}$ , (b)  $\tilde{Q}_e^{NL}$  and (c)  $\tilde{Q}_i^{NL}$  are compared with the quasilinear flux models (a)  $\tilde{\Gamma}_{ql}^{model}$ , (b)  $\tilde{Q}_{e,ql}^{model}$  and (c)  $\tilde{Q}_{i,ql}^{model}$  in Fig. 8, where the relative errors are given by (a) 2.3, (b) 0.24 and (c) 0.24. The relative error shown above for the particle flux model is larger than those for the energy fluxes, because the quasilinear particle flux becomes close to zero at some radial points. When using another definition<sup>34</sup> of the relative error  $\sqrt{\sum(\tilde{\Gamma}^{NL} - \tilde{\Gamma}_{ql}^{model})^2 / \sum(\tilde{\Gamma}_{ql}^{model})^2}$  for the particle fluxes at the twenty radial points, its value is as small as 0.3. For the ion energy flux model in Fig. 8(c), the values of the relative errors  $(\tilde{Q}_i^{NL}/\tilde{Q}_{i,ql}^{model} - 1)^2$  at  $\rho = 0.72$  for the high- $T_i$  plasmas and at  $\rho = 0.80$  for the low- $T_i$  plasmas ( $t = 1.9$ s) are about three or four times larger than the averaged value of the relative error for the all data points.

## VI. SUMMARY

The gyrokinetic equations for both electrons and ions are solved by numerical simulations to model the diffusivities and the fluxes for the particle and heat transport. First, the electron and ion heat diffusivities are evaluated from the nonlinear simulations for high- $T_i$  and low- $T_i$  plasmas in the LHD, where the ITG mode is destabilized. The model functions for the electron and ion heat diffusivities are shown in terms of the turbulent potential fluctuation  $\bar{\mathcal{T}}$  and the zonal flow potential fluctuation  $\bar{\mathcal{Z}}$ . Next, the linear gyrokinetic simulations are performed to estimate the linear growth rate and the zonal flow decay time. The two quantities  $\bar{\mathcal{T}}$  and  $\bar{\mathcal{Z}}$  in the model functions are approximated in terms of the quantity related with the mixing length estimate,  $\mathcal{L}$  and the zonal flow decay time,  $\tilde{\tau}_{ZF}$ . The

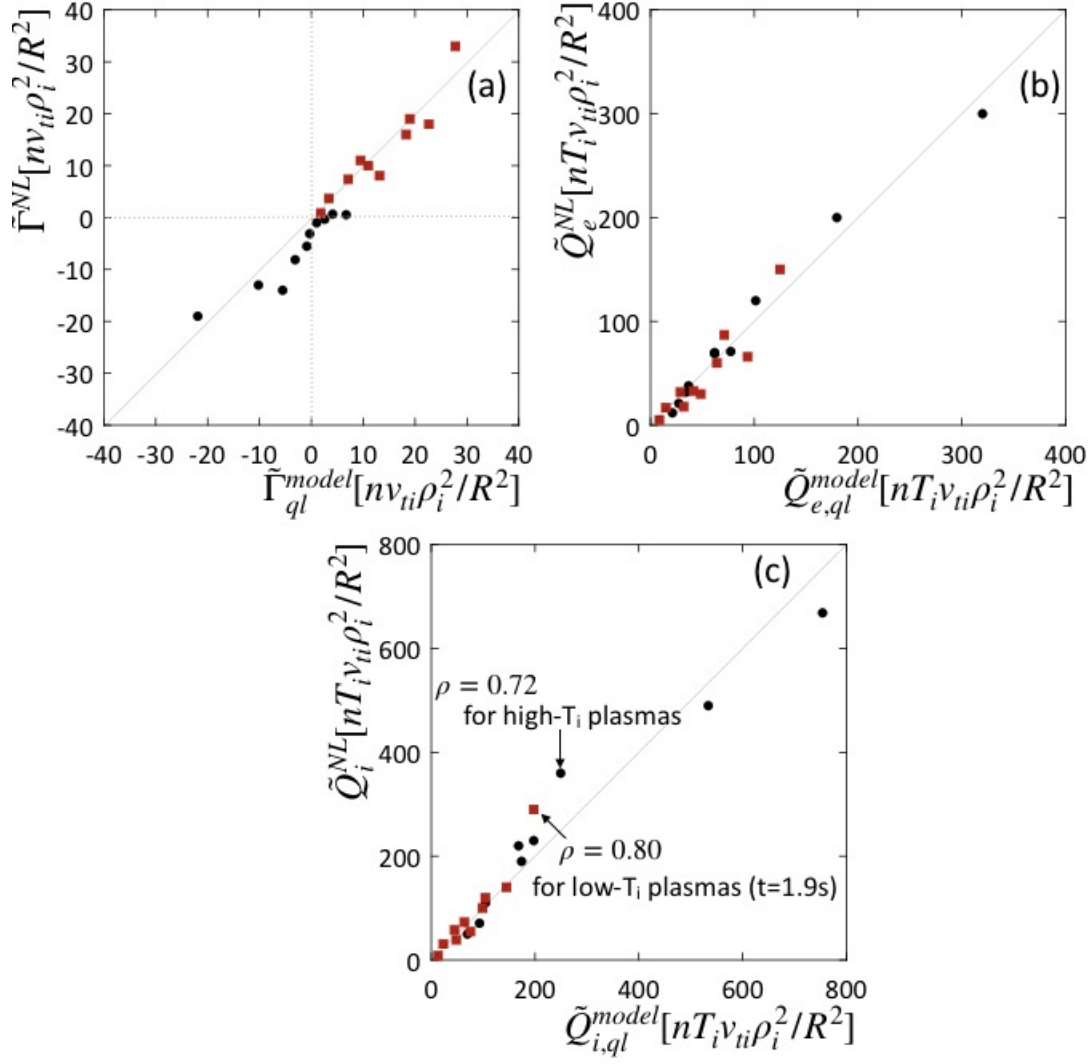


FIG. 8. The nonlinear simulation results for (a) the particle flux,  $\tilde{\Gamma}^{NL}$  (b) the electron energy flux,  $\tilde{Q}_e^{NL}$  and (c) ion energy flux,  $\tilde{Q}_i^{NL}$  are compared with the prediction by the quasilinear flux models,  $\tilde{\Gamma}_{ql}^{model}$ ,  $\tilde{Q}_{e,ql}^{model}$  and  $\tilde{Q}_{i,ql}^{model}$ . The circle and box marks show the cases for the high- $T_i$  and low- $T_i$  plasmas, respectively.

use of the linear simulation results enables us to reproduce the nonlinear simulation results for the electron and ion turbulent diffusivities by the heat diffusivity models shown in this article within the allowable errors. Since the density gradient is close to zero in some radial regions of the LHD plasmas, the reliable diffusivity model for the particle transport can not be shown. The quasilinear flux models for the electron and ion energy transport are proposed to quantitatively reproduce the nonlinear simulation results. The nonlinear simulation results of the electron and ion energy fluxes are reproduced by the quasilinear

flux models at the accuracy similar to that of the heat diffusivity models. In addition, the quasilinear particle flux model, which can be applicable even for the flattened density profiles in the LHD, is presented. Thus, the promising transport models, such as the heat diffusivity models and the quasilinear flux models for helical plasmas, are proposed based on the gyrokinetic simulation results. The quasilinear flux model for the particle transport can be proposed, while the particle diffusivity model cannot be shown. On the other hand, the heat diffusivity models are estimated by the two linear gyrokinetic simulation results,  $\mathcal{L}$  and  $\tau_{ZF}$ . When the quasilinear flux models are evaluated for the nonlinear simulation results, the ratio of the flux to fluctuating potential for the linear simulation is needed in addition to the two linear gyrokinetic simulation results. It is difficult to install the ratio of the flux to fluctuating potential for the linear simulation to the transport simulation code. How to apply the ion heat diffusivity model to the dynamical transport code was already reported<sup>22</sup> and the dynamical transport simulation result for the ion temperature profile will be compared with the experimental result in the LHD. The study on how to install the electron heat diffusivity model and the quasilinear flux models to the dynamical transport code is in progress and will be reported elsewhere.

How to construct the reduced models by use of the linear simulation results is explained for the low- $\beta$  plasmas. If the electromagnetic effect is important for high- $\beta$  plasmas, the reduced models by the linear simulation results will be studied. Reduced models of the turbulent transport in helical plasmas will be constructed in terms of the linear growth rate of the other modes, such as the trapped electron mode and the electron temperature gradient mode.

## ACKNOWLEDGMENTS

This work is partly supported by the NIFS Collaboration Research programs, NIFS18KNST129, NIFS18KNXN363 (Plasma Simulator), NIFS18KNTT045, the the JSPS KAKENHI Grant Number, 16K06941 and the Collaborative Research Program of Research Institute for Applied Mechanics, Kyushu University, 30FP-4.



## REFERENCES

- <sup>1</sup>J. W. Connor and H. R. Wilson, Plasma Phys. Control. Fusion **36**, 719 (1994).
- <sup>2</sup>W. Horton, Turbulence Transport in Magnetized Plasmas, 2nd ed. (World Scientific Pub. Co Inc; 2017).
- <sup>3</sup>X. Garbet, Y. Idomura, L. Villard and T. -H. Watanabe, Nucl. Fusion **50**, 0433002 (2010).
- <sup>4</sup>F. Jenko and W. Dorland, Plasma Phys. Control. Fusion **43**, A141 (2001).
- <sup>5</sup>J. Candy and R. E. Waltz, J. Comput. Phys. **186**, 545 (2003).
- <sup>6</sup>T. -H. Watanabe, H. Sugama and S. Ferrando-Margalet, Nucl. Fusion **47**, 1383 (2007).
- <sup>7</sup>P. Xanthopoulos, F. Merz, T. Görler, F. Jenko, Phys. Rev. Lett. **99**, 035002 (2007).
- <sup>8</sup>M. Nunami, T. -H. Watanabe, H. Sugama and K. Tanaka, Plasma Fusion Res. **6**, 1403001 (2011).
- <sup>9</sup>A. Ishizawa, T. -H. Watanabe, H. Sugama, S. Maeyama and N. Nakajima, Phys. Plasmas **21**, 055905 (2014).
- <sup>10</sup>M. Kotschenreuther, W. Dorland, M. A. Beer and G. W. Hammett, Phys. Plasmas **2**, 2381 (1995).
- <sup>11</sup>C. Holland, L. Schmitz, T. L. Rhodes, W. A. Peebles, J. C. Hillesheim, G. Wang, L. Zeng, E. J. Doyle, S. P. Smith, R. Prater, K. H. Burrell, J. Candy, R. E. Waltz, J. E. Kinsey, G. M. Staebler, J. C. DeBoo, C. C. Petty, G. R. McKee, Z. Yan and A. E. White, Phys. Plasmas **18**, 056113 (2011).
- <sup>12</sup>T. L. Rhodes, C. Holland, S. P. Smith, A. E. White, K. H. Burrell, J. Candy, J. C. DeBoo, E. J. Doyle, J. C. Hillesheim, J. E. Kinsey, G. R. McKee, D. Mikkelsen, W. A. Peebles, C. C. Petty, R. Prater, S. Parker, Y. Chen, L. Schmitz, G. M. Staebler, R.E. Waltz, G. Wang, Z. Yan and L. Zeng, Nucl. Fusion **51**, 063022 (2011).
- <sup>13</sup>M. Nunami, T. -H. Watanabe, H. Sugama and K. Tanaka, Phys. Plasmas **19**, 042504 (2012).
- <sup>14</sup>M. Nunami, T. -H. Watanabe and H. Sugama, Phys. Plasmas **20**, 092307 (2013).
- <sup>15</sup>J. Candy, C. Holland, R. E. Waltz, M. R. Fahey and E. Belli, Phys. Plasmas **16**, 060704 (2009).
- <sup>16</sup>M. Barnes, I. G. Abel, W. Dorland, T. Görler, G. W. Hammett and F. Jenko, Phys. Plasmas **17**, 056109 (2010).

- <sup>17</sup>M. Yokoyama, A. Wakasa, R. Seki, M. Sato, S. Murakami, C. Suzuki, Y. Nakamura, A. Fukuyama and LHD Experiment Group, Plasma Fusion Res. **7**, 2403011 (2012).
- <sup>18</sup>T. -H. Watanabe and H. Sugama, Nucl. Fusion **46**, 24 (2006).
- <sup>19</sup>M. Nunami, M. Nakata, S. Toda, A. Ishizawa, R. Kanno and H. Sugama, Phys. Plasmas **25**, 082504 (2018).
- <sup>20</sup>A. Ishizawa, T. -H. Watanabe, H. Sugama, M. Nunami, K. Tanaka, A. Maeyama and N. Nakajima, Nucl. Fusion **55**, 043024 (2015).
- <sup>21</sup>A. Ishizawa, Y. Kishimoto, T. -H. Watanabe, H. Sugama, K. Tanaka, S. Satake, S. Kobayashi, K. Nagasaki and Y. Nakamura, Nucl. Fusion **57**, 066010 (2017).
- <sup>22</sup>S. Toda, M. Nunami, A. Ishizawa, T. -H. Watanabe and H. Sugama, J. Phys.: Conf. Ser. **561**, 012020 (2014).
- <sup>23</sup>S. Toda, M. Nakata, M. Nunami, A. Ishizawa, T. -H. Watanabe and H. Sugama, Plasma and Fusion Research **12**, 1303035 (2017).
- <sup>24</sup>K. Tanaka, C. Micheal, L. Vyacheslavov, H. Funaba, M. Yokoyama, K. Ida, M. Yoshinuma, K. Nagaoka, S. Murakami, A. Wakasa, T. Ido, A. Shimizu, M. Nishimura, Y. Takeiri, O. Kaneko, K. Tsumori, K. Ikeda, M. Osakabe, K. Kawamata and LHD Experiment Group, Plasma Fusion Res. **5**, S2053 (2010).
- <sup>25</sup>H. Sugama and T. -H. Watanabe, Phys. Plasmas **13**, 012501 (2006).
- <sup>26</sup>S. Ferrando-Margalet, H. Sugama and T. -H. Watanabe, Phys. Plasmas **14**, 122505 (2007).
- <sup>27</sup>T. -H. Watanabe, H. Sugama and S. Ferrando-Margalet, Phys. Rev. Lett. **100**, 195002 (2008).
- <sup>28</sup>S. Toda, M. Nunami, S. Murakami, T. -H. Watanabe and H. Sugama, 20th International Stellarator-Heliotron Workshop 5-9 October 2015, Greifswald, Germany, P1S2-24 (2015)
- <sup>29</sup>J. Wesson, Tokamaks, 2nd ed. (Oxford University Press, 1997), p.198.
- <sup>30</sup>G. M. Stabler, J. E. Kinsey and R. E. Waltz, Phys. Plasmas **14**, 055909 (2007).
- <sup>31</sup>D. R. Mikkelsen, K. Tanaka, M. Nunami, T. -H. Watanabe, H. Sugama, M. Yoshinuma, K. Ida, Y. Suzuki, M. Goto, S. Morita, B. Wieland, I. Yamada, R. Yasuhara, T. Tokuzawa, T. Akiyama and N. A. Pablant, Phys. Plasmas **21**, 082302 (2014).
- <sup>32</sup>M. J. Pueschel, B. J. Faber, J. Citrin, C. C. Hegna, P. W. Terry and D. R. Hatch, Phys. Rev. Lett. **116**, 085001 (2016).
- <sup>33</sup>M. Nunami, M. Nakata, H. Sugama, K. Tanaka and S. Toda, Plasma Phys. Control. Fusion **59**, 044013 (2017).

<sup>34</sup>J. E. Kinsey, G. M. Stabler and R. E. Waltz, Phys. Plasmas **15**, 055908 (2008).